

Fig. 6. Comparison of clocking power estimated by post-layout simulation results.

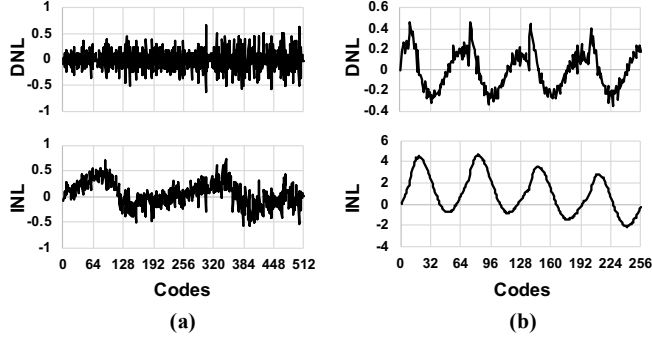


Fig. 7. Simulated DNL and INL of (a) DCDL and (b) PI.

VCO phase noise suppression.

### B. Proposed Clock Distribution Network

Fig. 5 shows the overall structure of the proposed CDR with a focus on the clock distribution network. Instead of distributing multi-phase high-frequency ( $4 \times 16$  GHz) clocks or a single-phase 16 GHz clock, the proposed CDR distributes a single-phase 1 GHz clock to minimize the distribution power. Within each lane, an injection-locked clock multiplier (ILCM) locally generates 4-phase 16 GHz clocks provided to local PIs for phase tracking. Power comparison, estimated based on post-layout simulation results, is presented in Fig. 6. We assume that the identical PIs are used for all cases, and the same ILO is utilized for multi-phase generation in the CDR with single-phase clock distribution. In Fig. 6, all the power values are normalized by the clock distribution power of the proposed CDR. Clocking power of the proposed RX is greatly reduced by 83% and 56%, respectively, which is attributed to the drastic reduction in global clock distribution power. We also note that, since single-phase high-frequency clock distribution requires additional hardware like ILO for multi-phase generation locally, distributing a low-frequency global clock and using local ILCMs that can multiply frequency as well as generate multi-phase clocks simultaneously with overhead similar to ILO, is more power-efficient.

In the proposed CDR, the FDIV, which consists of a multi-modulus divider (MMD), a gain-calibrated digitally-controlled delay line (DCDL), and a delta-sigma modulator (DSM) [21], compensates for the frequency error, instead of PI. The division ratio of the FDIV is controlled by accumulating the phase errors detected by the CDR logic, ensuring that local PIs get zero frequency offset clocks. This method provides two benefits: 1) the recovered clock shows lower deterministic jitter

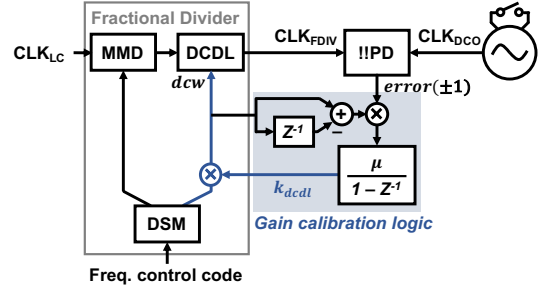


Fig. 8. DCDL gain calibration with LMS.

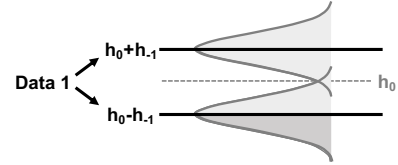


Fig. 9. Data-level distribution with white Gaussian noise.

(i.e., fractional spur) due to the superior linearity of the DCDL in FDIV over PI, and 2) the trade-off between the PI resolution and its ability to track larger frequency error is alleviated, as the PI no longer tracks frequency error. In addition, the collaborative collection of error information across all lanes increases the transition density (phase error detection density) effectively, thereby allowing RX to track frequency error more accurately compared to conventional baud-rate CDRs [22].

Fig. 7 highlights the enhanced linearity of DCDL compared to PI by comparing their differential non-linearity (DNL) and integral non-linearity (INL). DCDL demonstrates maximum DNL and INL of 0.68 LSB and 0.73 LSB, respectively, while PI exhibits 0.46 LSB and 4.67 LSB, respectively. Notably, DCDL achieves better linearity despite its finer phase step of 183 fs, compared to the PI's of 244 fs. Designing linear phase rotators has been a difficult task as discussed in Section II-A. Although prior art [23]-[26] has introduced effective phase rotators, they exhibit average DNL and INL of 0.68 LSB and 1.08 LSB, respectively, similar to or worse than those of DCDL, even with an average phase step of 719 fs, which emphasizes superior linearity of DCDL.

To minimize the phase error caused by FDIV, the range of DCDL must be equivalent to the period of the FDIV's input clock ( $CLK_{LC}$ ) under process, voltage, and temperature (PVT) variations [27]. Consequently, background calibration of the DCDL gain ( $k_{dcdl}$ ) is necessary. The calibration process employs the sign-sign least-mean-square (SS-LMS) algorithm, correlating the bang-bang PD (!!PD) output from ILCM with changes in the DCDL control code ( $dcw$ ), as illustrated in Fig. 8. Assuming the constant period of  $CLK_{FDIV}$  (ILCM input), the error from !!PD can be expressed as:

$$\begin{aligned} error = & (T_{mmd}[n] + k_{dcdl} \cdot dcw[n]) \\ & - (T_{mmd}[n+1] + k_{dcdl} \cdot dcw[n-1]), \end{aligned} \quad (1)$$

where  $T_{mmd}$  represents the period of the MMD output clock. Applying this error to the LMS algorithm leads to:

$$k_{dcdl}[n+1] = k_{dcdl}[n] - \mu \nabla_k error^2 \quad (2)$$

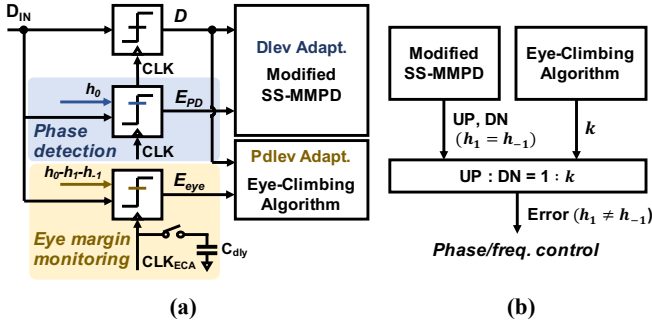


Fig. 10. (a) Three samplers for proposed CDR. (b) Phase update process.

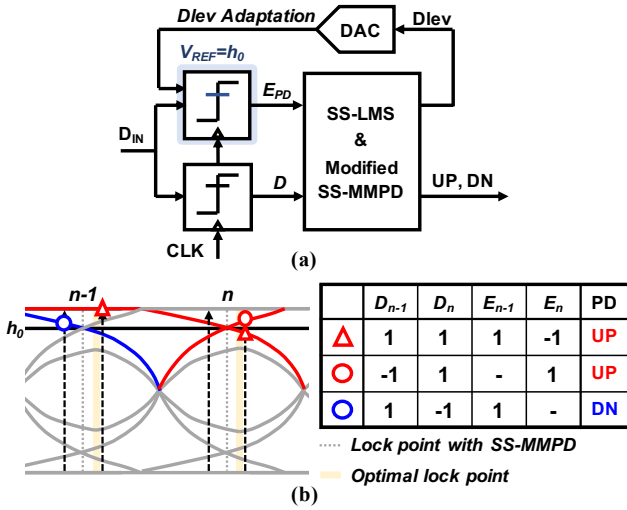


Fig. 11. (a) Phase detection in proposed CDR. (b) Phase detection logic.

$$k_{dcdl}[n+1] = k_{dcdl}[n] - \mu \cdot 2error \cdot (dcw[n] - dcw[n-1]). \quad (3)$$

By correlating the difference between the current  $dcw$  and the previous  $dcw$  with the error, it enables determination of an appropriate  $k_{dcdl}$  and ensures precise FDIV operation.

### III. CLOCK AND DATA RECOVERY

#### A. Issues in Prior Baud-Rate CDRs

Prior art has tried to address the issue of the sub-optimal lock point in conventional SS-MMPD-based CDRs [15]. For instance, [16] proposed an unequalized MMCDR that intentionally adds offset to enable phase lock at a point where  $h_1$  and  $h_{-1}$  do not coincide. Choosing a proper offset results in enhanced voltage margin, thereby improving BER. However, manually finding the optimal offset value, which is sensitive to channel characteristics, makes it difficult to use [16] in practice.

To mitigate this issue, [17] automatically search for the optimal offset by monitoring the eye height. When DFE removes all post-cursors and only the first precursor remains, data 1 can have two voltage levels,  $h_0 + h_{-1}$  and  $h_0 - h_{-1}$ , and the eye height can be represented as  $h_0 - h_{-1}$  (see Fig. 9). Then, by updating the data-level with LMS in 1:3 ratio, the adapted data-level converges to  $h_0 - h_{-1}$ , effectively indicating the eye height [28]. While sweeping the offset, this biased

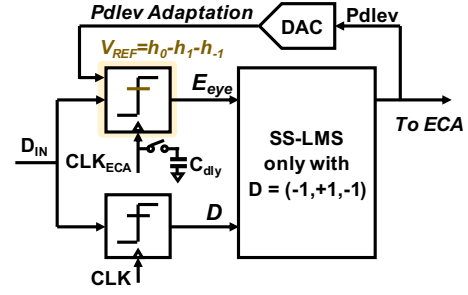


Fig. 12. Eye margin monitoring through Pdlev adaptation.

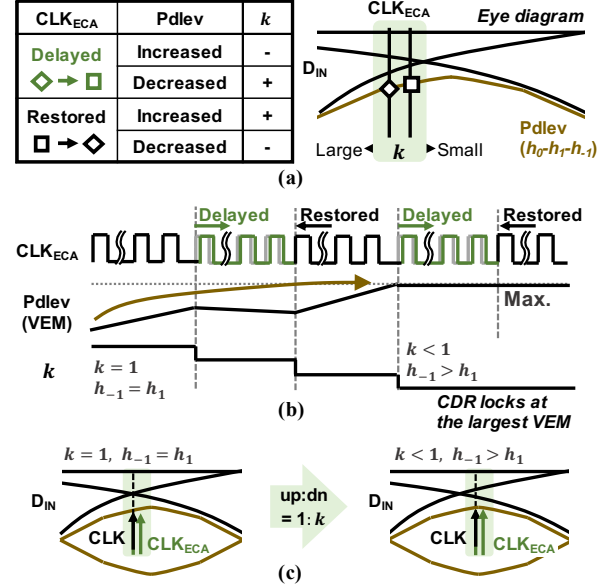


Fig. 13. (a) Operation principle and (b) transient example of proposed ECA. (c) Change of sampling clock phase.

data-level (Bdlev) adaptation can be utilized to identify the eye height corresponding to each offset and choose the one with the maximum eye height. However, this CDR also has several drawbacks. First, operating with only two samplers reduces the transition density to half that of the conventional SS-MMPD. Besides, using a single error sampler for both phase detection and Bdlev adaptation for eye height monitoring can cause interaction between two loops, resulting in undesirable dead zones. Second, when noise power is comparable to  $h_{-1}$ , the overlap region between the two levels increases as depicted in Fig. 9, which makes the Bdlev adaptation inadequate for accurately representing the effective eye height. Finally, while this method allows for automatic offset determination, it cannot operate robustly against PVT variations, necessitating a background calibration technique.

#### B. Proposed Baud-Rate CDR with ECA

The proposed baud-rate CDR operates with three samples per UI as shown in Fig. 10(a): One for data recovery, a second for SS-MM phase detection, and a third for eye margin monitoring. The phase detecting error sampler's outputs are used for data-level (Dlev) adaptation and modified SS-MMPD,

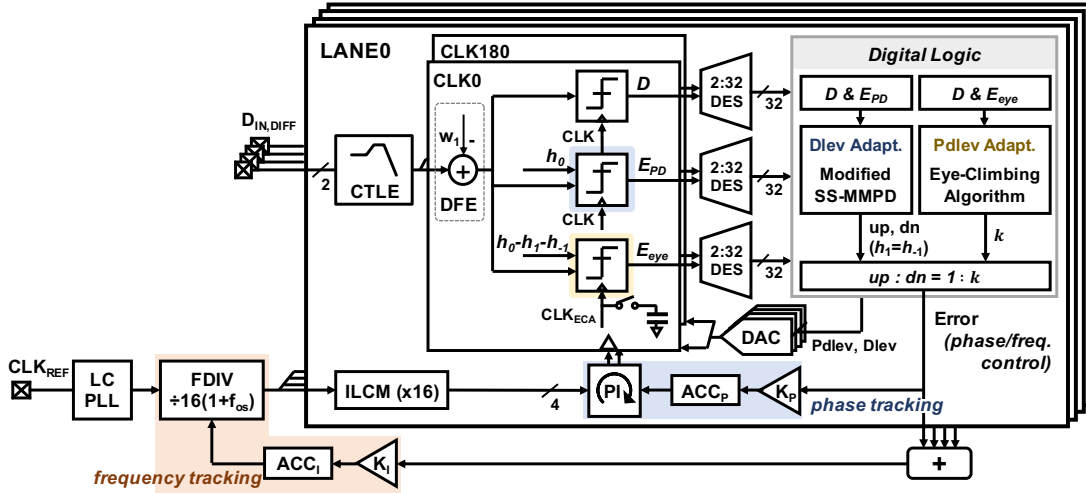


Fig. 14. Overall architecture of the proposed 4-lane CDR.

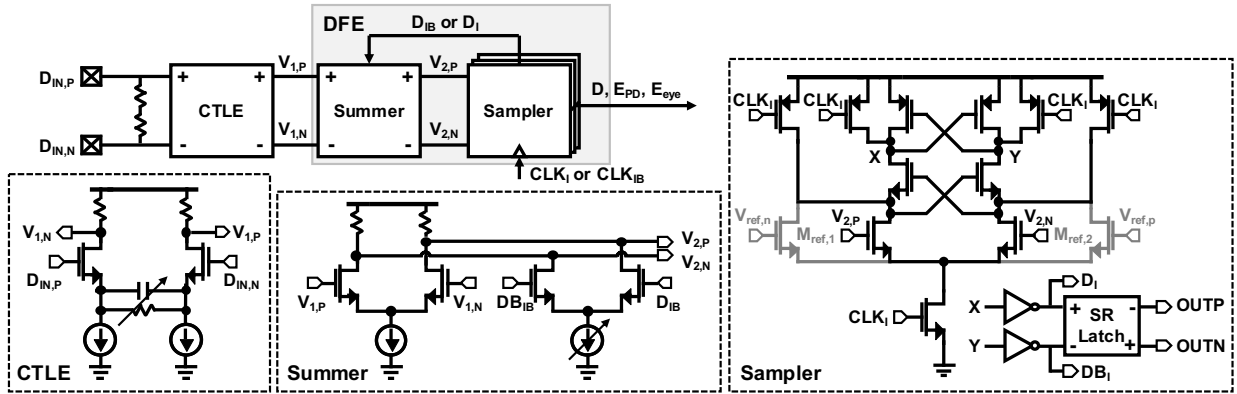


Fig. 15. Analog front-end implementation.

and the outputs of the eye monitoring sampler are for pattern-based data-level (Pdlev) adaptation indicating the eye margin. Fig. 10(b) shows the phase update process of the proposed CDR. Initially, CDR locks at the phase where  $h_1 = h_{-1}$  with modified SS-MMPD, employing only one error sampler. Subsequently, the clock phase update weight is changed to  $up : dn = 1 : k$  to adjust the recovered clock phase. The ratio or offset  $k$  is calibrated by the proposed ECA to ensure CDR locks at the largest VEM, maximizing Pdlev. Note that the clock phase ( $CLK_{ECA}$ ) for the eye margin monitoring sampler differs from  $CLK$  used in the other two samplers. Depending on whether the switch is on or not,  $CLK_{ECA}$  is either delayed or identical to  $CLK$ .

The proposed BRPD operates with just one error sampler and a data sampler but achieves higher transition density compared to other BRPDs with two samplers [17], [29], [30]. Fig. 11 demonstrates the operation of the modified SS-MMPD. The outputs from the error sampler ( $E_{PD}$ ) and the data sampler ( $D$ ) are utilized for phase error detection and Dlev adaptation. Dlev for the phase detection error sampler is adapted to  $h_0$  with the SS-LMS algorithm. Fig. 11(b) details the modification in the PD logic. By combining the error detection pattern from [15] and [17], it allows for phase error

detection in three cases with just two samplers, enhancing the transition density compared to conventional BRPDs with two samplers<sup>1</sup>.

For eye height estimation, the eye monitoring sampler's reference voltage (Pdlev) is adapted through SS-LMS, updated only with the data pattern  $(-1, +1, -1)$ , as shown in Fig. 12. This makes Pdlev converge to  $h_0 - h_1 - h_{-1}$ , which represents the effective VEM. The input of the samplers,  $D_{IN}$ , can be expressed as convolution between data  $x_n$  and channel's impulse response  $h_n$ :

$$D_{IN,n} = \sum (x_{n-k} h_k) = \dots + h_1 x_{n-1} + h_0 x_n + h_{-1} x_{n+1} + \dots \quad (4)$$

The SS-LMS algorithm applied with the pattern of  $(-1, 1, -1)$  finds Pdlev ( $w_0$ ), which minimizes the expression:

$$\sum_n (D_{IN,n} - w_0 x_n)^2 = (\dots + h_1 x_{n-1} + h_0 x_n + h_{-1} x_{n+1} + \dots - w_0 x_n)^2 \quad (5) = (\dots - h_1 + h_0 - h_{-1} + \dots - w_0)^2.$$

<sup>1</sup>Since the DFE removes post-cursors, the pattern  $(D_{n-1}, D_n, E_{n-1}, E_n) = (1, 1, -1, 1)$  does not occur. Thus, there are more patterns for detecting  $up$  than for detecting  $dn$ .



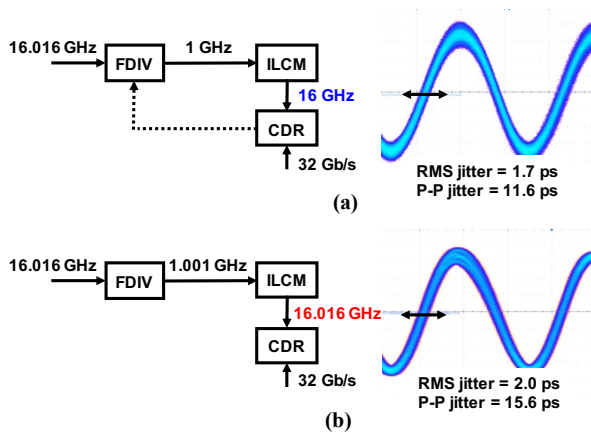


Fig. 19. Measured recovered clock jitter with 1000 ppm frequency offset: (a) Frequency tracking with FDIV. (b) Frequency tracking only with PI.

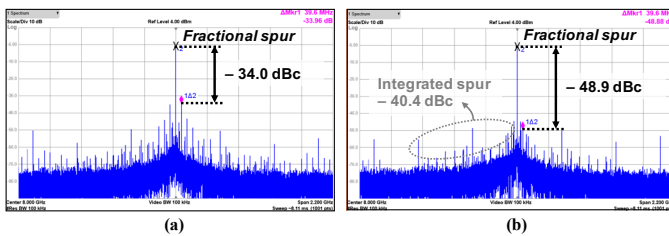


Fig. 20. Measured fractional spur of ILCM output with 2500 ppm frequency offset (a) before DCDL gain calibration and (b) after DCDL gain calibration.

### C. Local Clock Path

In each lane, the ILCM converts the distributed low-frequency clock into high-frequency multi-phase clocks, and the local PIs adjust the phase to generate the recovered clock. Fig. 17 details the structure of ILCM. As in [36], ILCM employs the gating approach to track the frequency of the reference clock and address delay mismatch through a de-skewing loop, alleviating reference spur. However, the de-skewing loop in the ILCM operates when the injection pulse is gated, differing from [36] where the frequency tracking loop operates during pulse injection. For phase tracking, 8-bit current-mode PIs are implemented with seamless switching [37] and controlled by the CDR proportional path.

## V. MEASUREMENT RESULTS

The prototype 4-lane RX is fabricated in a 28 nm CMOS and occupies an active area of  $0.42 \text{ mm}^2$  as shown in Fig. 18. The entire RX consumes 232 mW (58 mW per lane) with the aggregate data rate of 128 Gb/s. Fig. 18(b) shows the area and power breakdown of the entire RX.

### A. Clocking Performance

The proposed multi-lane RX efficiently distributes a low-frequency single-phase clock over a 2 mm distance, consuming only 6.76 mW. Moreover, thanks to the good DCDL linearity in FDIV, the recovered clock shows better jitter performance than PI-based CDR in the presence of frequency offset, which is demonstrated in Fig. 19 (measured with a 1000 ppm

TABLE I  
PERFORMANCE COMPARISON WITH OTHER MULTI-PHASE GENERATING PHASE ROTATORS.

	ISSCC'19 [25]	ISSCC'21 [26]	This Work
Technology	16 nm	65 nm	28 nm
Architecture	ILPR	MPILOSC	FDIV+ ILCM
Resolution [bits]	8	7	9
Power [mW]	11.4 @ 7 GHz	15.6 @ 7 GHz	16.0 @ 16 GHz
Power/GHz [mW/GHz]	1.63	2.23	1
Integrated Fractional Spurs	-39.4 dBc @ -1300 ppm	-33.9 dBc @ 1000 ppm	-40.4 dBc @ 2500 ppm

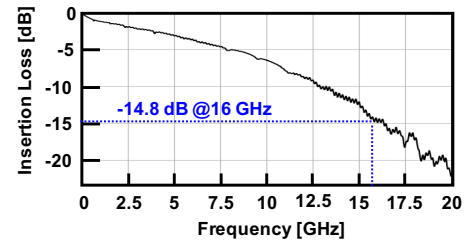


Fig. 21. Measured insertion loss of the channel.

frequency offset). As shown in Fig. 19(a), the proposed CDR, where the FDIV tracks frequency offset and the PIs only cover phase error, shows the recovered clock jitter of  $1.7 \text{ ps}_{\text{rms}}$  and  $11.6 \text{ ps}_{\text{p2p}}$ . On the other hand, if the frequency offset is tracked only by PIs as in conventional CDRs<sup>2</sup>, jitter increase to  $2.0 \text{ ps}_{\text{rms}}$  and  $15.6 \text{ ps}_{\text{p2p}}$  (see Fig. 19(b)). Fig. 20 shows the measured spectra of the ILCM output with a 2500 ppm frequency offset (FDIV division ratio fixed at 16.04), where fractional spurs due to DCDL non-linearity can be observed. Without DCDL gain calibration, fractional spur of  $-34.0 \text{ dBc}$  appears at 40 MHz due to large phase-domain quantization error. However, with the LMS-based gain calibration, this spur is reduced to  $-48.9 \text{ dBc}$ . Table I compares the performance of the proposed frequency tracking scheme with other state-of-the-art multi-phase generating phase rotators [25], [26]. Thanks to the superior DCDL linearity in FDIV, the lowest integrated fractional spur is achieved with excellent clocking power efficiency of  $1 \text{ mW/GHz}$ .

### B. RX Performance

The RX performance at 32 Gb/s was measured with a 15 dB channel loss including SMA cable and FR-4 trace loss. Fig. 21 depicts the tested channel characteristic. As shown in Fig. 22, the measured JTOL corner frequency is 10 MHz, and the measured recovered clock jitter is  $1.3 \text{ ps}_{\text{rms}}$  and  $8.8 \text{ ps}_{\text{p2p}}$ , respectively. Fig. 23 shows the measured BER bathtub curves for each lane of the proposed 4-lane RX. The effectiveness of the proposed ECA is validated by comparing BER when ECA is on/off. For lane0, with the conventional timing recovery (ECA off), the recovered clock phase locks at  $-0.09 \text{ UI}$  apart from the proposed CDR's sampling phase, which results in

<sup>2</sup>To mimic the PI behavior in conventional CDRs, the control code for FDIV is fixed as shown in Fig 19(b).

TABLE II  
PERFORMANCE SUMMARY AND COMPARISON WITH HIGH-SPEED NRZ RXS.

	ISSCC'15 [16]	VLSI'20 [17]	ISSCC'17 [21]	ISSCC'16 [30]	JSSC'23 [38]	This work
Technology	14 nm	28 nm	65 nm	28 nm	22 nm	28 nm
Phase Detection	Unequalized SS-MMPD	SS-MMPD with MET	2x-Oversampling	Pattern Based BRPD	2x-Oversampling	<b>SS-MMPD with ECA</b>
Clock Recovery	PI*	PI*	FDIV + MDLL	VCO	PLL + PI*	FDIV + PI*
# of Lanes	2	1	1	2	1	<b>4</b>
Data Rate [Gb/s]	10	28	10	56.2	26	32
Aggregate Data Rate [Gb/s]	20	28	10	112.4	26	<b>128</b>
Channel Loss [dB]	24	20	NaN	18.4	32	15
Equalization	CTLE 4-tap DFE	CTLE 2-tap DFE	CTLE VGA	CTLE 1-tap DFE	CTLE 4-tap DFE	CTLE 1-tap DFE
Active Area [mm <sup>2</sup> /lane]	0.065**	0.108	0.383	0.141	0.073	0.105
RX Clocking Power Efficiency [mW/Gb/s]	1.24**	0.51	0.92	N/A	0.73	<b>0.65</b>
Energy Efficiency [pJ/bit]	5.9**	2.02	2.59	2.53	3.3	<b>1.81</b>

\* CML PI \*\* Transceiver

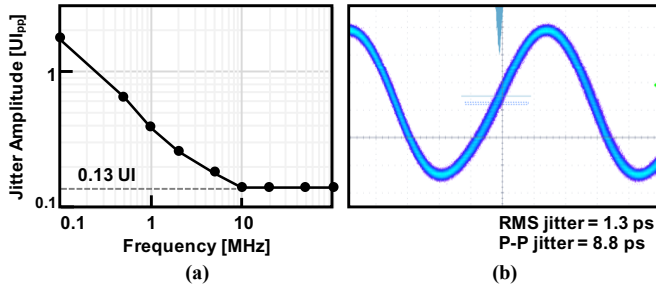


Fig. 22. Measured (a) jitter tolerance and (b) recovered clock of the proposed CDR.

the degraded BER of  $3 \times 10^{-10}$ . On the other hand, the proposed CDR shifts the lock point with ECA, achieving error-free operation ( $BER < 10^{-12}$ ) and a 17% increase in VEM compared to that of the conventional CDR. Across all lanes, BER improves from  $3 \times 10^{-10}$ ,  $4 \times 10^{-12}$ ,  $1.5 \times 10^{-9}$ , and  $8 \times 10^{-12}$  in conventional CDR to  $BER < 10^{-12}$  with the proposed method. In addition, VEMs of four lanes are increased by 17%, 8%, 10%, 8%, respectively, thanks to ECA. In Table II, performance comparison with other recently published high-speed NRZ RXs is provided. Although other works implements fewer (one or two) lanes and a shorter-distance clock distribution, thanks to the novel low-power global clock distribution technique, the proposed 4-lane RX achieves the best energy efficiency.

## VI. CONCLUSION

In multi-lane high-speed RXs, the clocking scheme plays a crucial role in determining overall RX power consumption. This paper presents design techniques for an energy-efficient multi-lane baud-rate CDR. The proposed CDR achieves substantial power savings with an energy-efficient clocking scheme, employing a low-frequency single-phase global clock distribution and baud-rate recovery. Frequency offset

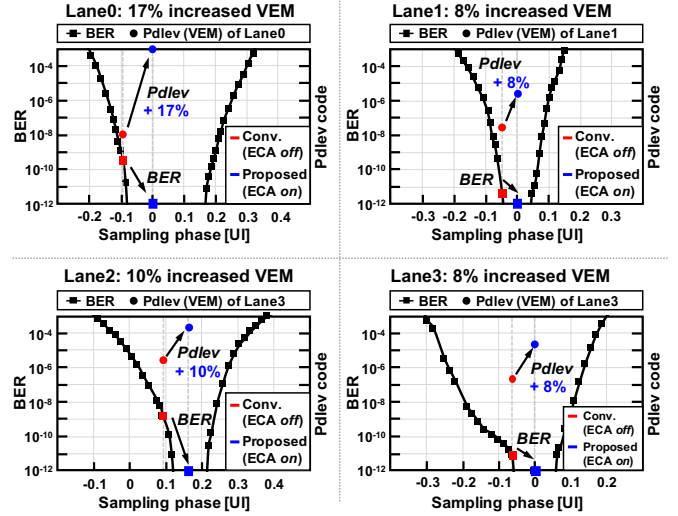


Fig. 23. Measured BER bathtub curves of each lane.

is compensated by FDIV before global clock distribution, which leads to reduced deterministic jitter in the recovered clock typically caused by PI non-linearity. In addition, the proposed background ECA successfully addresses the lock point issue of the conventional BRPDs, thereby improving both VEM and BER. This enhancement is achieved without requiring additional hardware. The prototype  $4 \times 32$  Gb/s RX fabricated in a 28 nm CMOS process demonstrates superior energy efficiency of 1.8 pJ/bit even with a long-distance clock distribution of 2 mm. Thanks to the frequency-tracking FDIV, the RX achieves a low integrated fractional spur of -40.4 dBc with a 2500 ppm frequency offset. Furthermore, the proposed ECA contributes to 17% increase in VEM compared to conventional methods, ensuring robust and error-free operation of the proposed RX.

## ACKNOWLEDGMENT

The EDA tool was supported by the IC Design Education Center (IDEC), Korea.

## REFERENCES

- [1] B. Zhang *et al.*, “A 112Gb/s serial link transceiver with 3-tap FFE and 18-tap DFE receiver for up to 43dB insertion loss channel in 7nm FinFET technology,” in *2023 IEEE International Solid-State Circuits Conference (ISSCC)*. IEEE, 2023, pp. 5–7.
- [2] N. Kocaman *et al.*, “An 182mW 1-60Gb/s configurable PAM-4/NRZ transceiver for large scale ASIC integration in 7nm FinFET technology,” in *2022 IEEE International Solid-State Circuits Conference (ISSCC)*, vol. 65. IEEE, 2022, pp. 120–122.
- [3] M.-A. LaCroix *et al.*, “A 116Gb/s DSP-based wireline transceiver in 7nm CMOS achieving 6pJ/b at 45dB loss in PAM-4/Duo-PAM-4 and 52dB in PAM-2,” in *2021 IEEE International Solid-State Circuits Conference (ISSCC)*, vol. 64. IEEE, 2021, pp. 132–134.
- [4] B.-J. Yoo *et al.*, “A 56Gb/s 7.7 mW/Gb/s PAM-4 wireline transceiver in 10nm FinFET using MM-CDR-Based ADC timing skew control and low-power DSP with approximate multiplier,” in *2020 IEEE International Solid-State Circuits Conference-ISSCC*. IEEE, 2020, pp. 122–124.
- [5] N. Kocaman *et al.*, “A 3.8 mW/Gbps quad-channel 8.5–13 Gbps serial link with a 5 tap DFE and a 4 tap transmit FFE in 28 nm cmos,” *IEEE Journal of Solid-State Circuits*, vol. 51, no. 4, pp. 881–892, 2016.
- [6] B. Raghavan *et al.*, “A sub-2W 39.8-to-44.6Gb/s transmitter and receiver chipset with SFI-5.2 interface in 40nm CMOS,” in *2013 IEEE International Solid-State Circuits Conference-ISSCC*. IEEE, 2013, pp. 32–33.
- [7] U. Singh *et al.*, “A 780mW 4x28Gb/s transceiver for 100GbE Gearbox PHY in 40nm CMOS,” in *2014 IEEE International Solid-State Circuits Conference-ISSCC*. IEEE, 2014, pp. 40–41.
- [8] J. Pangjun and S. S. Sapatnekar, “Low-power clock distribution using multiple voltages and reduced swings,” *IEEE Transactions on Very Large Scale Integration (VLSI) Systems*, vol. 10, no. 3, pp. 309–318, 2002.
- [9] B. Casper and F. O’Mahony, “Clocking analysis, implementation and measurement techniques for high-speed data links—a tutorial,” *IEEE Transactions on Circuits and Systems I: Regular Papers*, vol. 56, no. 1, pp. 17–39, 2009.
- [10] S. Saxena, G. Shu, R. K. Nandwana, M. Talegaonkar, A. Elkholy, T. Anand, W.-S. Choi, and P. K. Hanumolu, “A 2.8 mW/Gb/s, 14 Gb/s serial link transceiver,” *IEEE Journal of Solid-State Circuits*, vol. 52, no. 5, pp. 1399–1411, 2017.
- [11] S. Park, Y. Choi, J. Sim, J. Choi, H. Park, Y. Kwon, and C. Kim, “A 0.83 pJ/b 52Gb/s PAM-4 baud-rate CDR with pattern-based phase detector for short-reach applications,” in *2023 IEEE International Solid-State Circuits Conference (ISSCC)*. IEEE, 2023, pp. 118–120.
- [12] Y. Segal, A. Laufer, A. Khairi, Y. Krupnik, M. Cusmai, I. Levin, A. Gordon, Y. Sabag, V. Rahinski, G. Ori *et al.*, “A 1.41 pJ/b 224Gb/s PAM-4 SerDes receiver with 31dB loss compensation,” in *2022 IEEE International Solid-State Circuits Conference (ISSCC)*, vol. 65. IEEE, 2022, pp. 114–116.
- [13] B. Ye, K. Sheng, W. Gai, H. Niu, B. Zhang, Y. He, S. Jia, C. Chen, and J. Yu, “A 2.29 pJ/b 112Gb/s wireline transceiver with RX 4-tap FFE for medium-reach applications in 28nm CMOS,” in *2022 IEEE International Solid-State Circuits Conference (ISSCC)*, vol. 65. IEEE, 2022, pp. 118–120.
- [14] J. Bailey, H. Shakiba, E. Nir, G. Marderfeld, P. Krotnev, M.-A. LaCroix, and D. Cassan, “A 112Gb/s PAM-4 low-power 9-tap sliding-block DFE in a 7nm FinFET wireline receiver,” in *2021 IEEE International Solid-State Circuits Conference (ISSCC)*, vol. 64. IEEE, 2021, pp. 140–142.
- [15] F. Spagna, L. Chen, M. Deshpande, Y. Fan, D. Gambetta, S. Gowder, S. Iyer, R. Kumar, P. Kwok, R. Krishnamurthy *et al.*, “A 78mW 11.8 Gb/s serial link transceiver with adaptive RX equalization and baud-rate CDR in 32nm CMOS,” in *2010 IEEE International Solid-State Circuits Conference-ISSCC*. IEEE, 2010, pp. 366–367.
- [16] R. Dokania, A. Kern, M. He, A. Faust, R. Tseng, S. Weaver, K. Yu, C. Bil, T. Liang, and F. O’Mahony, “A 5.9 pJ/b 10Gb/s serial link with unequalized MM-CDR in 14nm tri-gate CMOS,” in *2015 IEEE International Solid-State Circuits Conference-ISSCC Digest of Technical Papers*. IEEE, 2015, pp. 1–3.
- [17] M.-C. Choi, H.-G. Ko, J. Oh, H.-Y. Joo, K. Lee, and D.-K. Jeong, “A 0.1-pJ/b/dB 28-Gb/s maximum-eye tracking, weight-adjusting MM CDR and adaptive DFE with single shared error sampler,” in *2020 IEEE Symposium on VLSI Circuits*. IEEE, 2020, pp. 1–2.
- [18] J. F. Bulzacchelli, M. Meghelli, S. V. Rylov, W. Rhee, A. V. Rylyakov, H. A. Ainspan, B. D. Parker, M. P. Beakes, A. Chung, T. J. Beukema *et al.*, “A 10-Gb/s 5-tap DFE/4-tap FFE transceiver in 90-nm CMOS technology,” *IEEE Journal of Solid-State Circuits*, vol. 41, no. 12, pp. 2885–2900, 2006.
- [19] P. K. Hanumolu, G.-Y. Wei, and U.-K. Moon, “A wide-tracking range clock and data recovery circuit,” *IEEE Journal of Solid-State Circuits*, vol. 43, no. 2, pp. 425–439, 2008.
- [20] M. Hossain, E.-H. Chen, R. Navid, B. Leibowitz, A. Chou, S. Li, M.-J. Park, J. Ren, B. Daly, B. Su *et al.*, “A 4 × 40 gb/s quad-lane cdr with shared frequency tracking and data dependent jitter filtering,” in *2014 Symposium on VLSI Circuits Digest of Technical Papers*. IEEE, 2014, pp. 1–2.
- [21] R. K. Nandwana, S. Saxena, A. Elkholy, M. Talegaonkar, J. Zhu, W.-S. Choi, A. Elmallah, and P. K. Hanumolu, “A 3-to-10Gb/s 5.75 pJ/b transceiver with flexible clocking in 65nm CMOS,” in *2017 IEEE International Solid-State Circuits Conference (ISSCC)*. IEEE, 2017, pp. 492–493.
- [22] A. Agrawal, A. Liu, P. K. Hanumolu, and G.-Y. Wei, “An 8 × 5 Gb/s parallel receiver with collaborative timing recovery,” *IEEE journal of solid-state circuits*, vol. 44, no. 11, pp. 3120–3130, 2009.
- [23] S. Chen, L. Zhou, I. Zhuang, J. Im, D. Melek, J. Namkoong, M. Raj, J. Shin, Y. Frans, and K. Chang, “A 4-to-16ghz inverter-based injection-locked quadrature clock generator with phase interpolators for multi-standard i/os in 7nm finfet,” in *2018 IEEE International Solid-State Circuits Conference - (ISSCC)*, 2018, pp. 390–392.
- [24] E. Monaco, G. Anzalone, G. Albasini, S. Erba, M. Bassi, and A. Mazzanti, “A 2–11 ghz 7-bit high-linearity phase rotator based on wideband injection-locking multi-phase generation for high-speed serial links in 28-nm cmos fdsoi,” *IEEE Journal of Solid-State Circuits*, vol. 52, no. 7, pp. 1739–1752, 2017.
- [25] Y.-C. Huang and B.-J. Chen, “An 8b injection-locked phase rotator with dynamic multiphase injection for 28/56/112Gb/s serdes application,” in *2019 IEEE International Solid-State Circuits Conference-ISSCC*. IEEE, 2019, pp. 486–488.
- [26] Z. Wang, Y. Zhang, Y. Onizuka, and P. R. Kinget, “A high-accuracy multi-phase injection-locked 8-phase 7GHz clock generator in 65nm with 7b phase interpolators for high-speed data links,” in *2021 IEEE International Solid-State Circuits Conference (ISSCC)*, vol. 64. IEEE, 2021, pp. 186–188.
- [27] A. Elkholy, T. Anand, W.-S. Choi, A. Elshazly, and P. K. Hanumolu, “A 3.7 mW low-noise wide-bandwidth 4.5 GHz digital fractional-N PLL using time amplifier-based TDC,” *IEEE Journal of Solid-State Circuits*, vol. 50, no. 4, pp. 867–881, 2015.
- [28] H.-Y. Joo, J. Lee, H. Ju, H.-G. Ko, J. M. Yoon, B. Kang, and D.-K. Jeong, “A maximum-eye-tracking CDR with biased data-level and eye slope detector for near-optimal timing adaptation,” *IEEE Transactions on Very Large Scale Integration (VLSI) Systems*, vol. 28, no. 12, pp. 2708–2720, 2020.
- [29] T. Shibasaki, W. Chaivipas, Y. Chen, Y. Doi, T. Hamada, H. Takauchi, T. Mori, Y. Koyanagi, and H. Tamura, “A 56-Gb/s receiver front-end with a CTLE and 1-tap DFE in 20-nm CMOS,” in *2014 Symposium on VLSI Circuits Digest of Technical Papers*. IEEE, 2014, pp. 1–2.
- [30] T. Shibasaki, T. Danjo, Y. Ogata, Y. Sakai, H. Miyaoka, F. Terasawa, M. Kudo, H. Kano, A. Matsuda, S. Kawai *et al.*, “A 56Gb/s NRZ-electrical 247mW/lane serial-link transceiver in 28nm CMOS,” in *2016 IEEE International Solid-State Circuits Conference (ISSCC)*. IEEE, 2016, pp. 64–65.
- [31] B. Razavi, “The design of an equalizer—part one [the analog mind],” *IEEE Solid-State Circuits Magazine*, vol. 13, no. 4, pp. 7–160, 2021.
- [32] —, “The decision-feedback equalizer [a circuit for all seasons],” *IEEE Solid-State Circuits Magazine*, vol. 9, no. 4, pp. 13–132, 2017.
- [33] —, “The design of a comparator [the analog mind],” *IEEE Solid-State Circuits Magazine*, vol. 12, no. 4, pp. 8–14, 2020.
- [34] A. Elkholy, S. Saxena, R. K. Nandwana, A. Elshazly, and P. K. Hanumolu, “A 2.0–5.5 GHz wide bandwidth ring-based digital fractional-n pll with extended range multi-modulus divider,” *IEEE Journal of Solid-State Circuits*, vol. 51, no. 8, pp. 1771–1784, 2016.
- [35] A. Elmallah, M. G. Ahmed, A. Elkholy, W.-S. Choi, and P. K. Hanumolu, “A 1.6ps peak-INL 5.3ns range two-step digital-to-time converter in 65nm CMOS,” in *2018 IEEE Custom Integrated Circuits Conference (CICC)*, 2018, pp. 1–4.
- [36] A. Elkholy, M. Talegaonkar, T. Anand, and P. K. Hanumolu, “Design and analysis of low-power high-frequency robust sub-harmonic injection-locked clock multipliers,” *IEEE Journal of Solid-State Circuits*, vol. 50, no. 12, pp. 3160–3174, 2015.

- [37] M. Talegaonkar, T. Anand, A. Elkholy, A. Elshazly, R. K. Nandwana, S. Saxena, B. Young, W.-S. Choi, and P. K. Hanumolu, "A 5GHz digital fractional- $N$  PLL using a 1-bit delta-sigma frequency-to-digital converter in 65 nm CMOS," *IEEE Journal of Solid-State Circuits*, vol. 52, no. 9, pp. 2306–2320, 2017.
- [38] Y.-C. Liu, W.-Z. Chen, Y.-S. Lee, Y.-H. Chen, S. Ming, and Y.-H. Lin, "A 103 fJ/b/dB, 10–26 Gb/s receiver with a dual feedback nested loop cdr for wide bandwidth jitter tolerance enhancement," *IEEE Journal of Solid-State Circuits*, 2023.